Applied Energy 357 (2024) 122512

Contents lists available at ScienceDirect

Applied Energy

journal homepage: www.elsevier.com/locate/apenergy

Triboelectric-electromagnetic hybrid generator with Savonius flapping wing for low-velocity water flow energy harvesting

Jiacheng Zhang [a,b,1], Yang Yu [b,c,1], Hengyu Li [b,c,1], Mingkang Zhu [a,b], Sheng Zhang [b,c], Chengjie Gu [d], Lin Jiang [a], Zhong Lin Wang [b,e,*], Jianyang Zhu [a,b,*], Tinghai Cheng [b,c,*]

[a] Wuhan University of Science and Technology, Wuhan 430081, China
[b] Beijing Institute of Nanoenergy and Nanosystems, Chinese Academy of Sciences, Beijing 101400, China
[c] School of Nanoscience and Engineering, University of Chinese Academy of Sciences, Beijing 100049, China
[d] Anhui University of Science and Technology, Hefei 231131, China
[e] Yonsei Frontier Lab, Yonsei University, Seoul 03722, Republic of Korea

HIGHLIGHTS

- A triboelectric-electromagnetic hybrid generator based on savonius flapping wing is proposed to harvest water flow energy.
- A pitching mechanism is designed to decouple the pitching and flapping of SFW, which can harvest the low-velocity water flow energy.
- A ratchet-gear-rack mechanism is used to convert the low-frequency flapping of SFW into the high-frequency rotation of TEHG.
- A power supply system based on the SFW-TEHG is built to power wireless sensors for realizing self-powered monitoring.

GRAPHICAL ABSTRACT

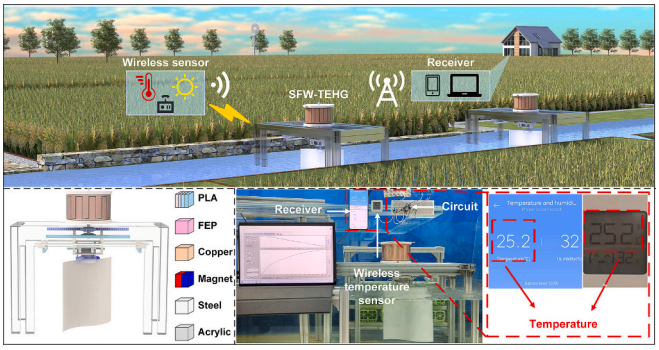

ARTICLE INFO

Keywords:
Triboelectric nanogenerator
Flapping wing
Low-velocity water flow
Energy harvesting
Electromagnetic generator

ABSTRACT

Low-velocity water flow exists generally in open channel environments, and harvesting energy from these water flows remains a challenge. Herein, a savonius flapping wing triboelectric–electromagnetic hybrid generator (SFW-TEHG) is proposed to harvest the low-velocity water flow energy by the reciprocating flapping of the savonius flapping wing. Whereafter, the reciprocating flapping is converted into the high-frequency rotating of the energy conversion part by the symmetrical distributed ratchet-gear-rack compound transmission mechanism, thus realizing the conversion of hydrokinetic energy into electricity. Under the water flow velocity of 0.21 m/s, the open-circuit voltage peak and the short-circuit current peak of the TENG reach 1.57 kV and 30.94 μA, and that of the EMG reach 6.24 V and 3.76 mA, respectively. In application demonstration, the SFW-TEHG can drive wireless sensors to monitor the environment. The SFW-TEHG furnishes a solution for the difficulty of harvesting low-velocity water flow energy and powering microsensors installed widely.

* Corresponding authors at: Beijing Institute of Nanoenergy and Nanosystems, Chinese Academy of Sciences, Beijing 101400, China.
E-mail addresses: zhong.wang@mse.gatech.edu (Z.L. Wang), zhujy@wust.edu.cn (J. Zhu), chengtinghai@binn.cas.cn (T. Cheng).
[1] These authors contributed equally to this work.

https://doi.org/10.1016/j.apenergy.2023.122512
Received 12 September 2023; Received in revised form 9 December 2023; Accepted 14 December 2023
Available online 25 December 2023

1. Introduction

As Internet of Things (IoT) advances rapidly in the smart agricultural sector [1], the demand for deploying microsensors in outdoor environments has surged [2]. These sensors are deployed extensively and in large quantities [3]. However, the traditional energy supply approaches such as cable wiring and batteries [4] will bring pollution and ecological environment damage. Therefore, utilizing renewable energy sources for supplying these microsensors is an appropriate solution. As a renewable energy source, hydrokinetic energy exhibits several notable advantages including widespread availability, operational stability, and high energy density [5]. The efficient conversion of hydrokinetic energy into electricity holds significant promise for effectively resolving the power supply problems caused by these sensors [6–8]. Nevertheless, most water flows are open and unidirectional in natural environments, and the flow velocity is about 1 m/s or less [9], which poses a significant challenge in harvesting the low-velocity water flow energy. Hence, a novel technology that can integrate seamlessly with existing techniques is in demand urgently, thereby offering innovative solutions for efficiently harvesting and harnessing the low-velocity water flow energy.

Triboelectric nanogenerator (TENG) based on the coupling of triboelectric effect and electrostatic induction [10] was invented by Wang's group in 2012 [11]. The TENG offers four operational modes, which makes it enable to convert mechanical energy into electricity [12–14] in diverse environments [15–20]. The TENG offers a broad selection of materials [21–24], allowing for cost-effective fabrication [25,26]. Furthermore, it has been verified that many TENGs are suitable for harvesting the low-frequency and the weak energy [27,28], which contributes to roundly harvesting clean energy. Currently, many TENGs are developed to harvest and convert water flow energy into electricity [29–31], which include water turbine type, waterwheel type, and vibration type. These types of TENGs have greatly promoted the development of water flow energy harvesting. However, these TENGs only harvest a tiny amount of energy and even can't start up when operate in low-velocity water flow [32,33].

The flapping wing is a front-end energy harvesting structure that is inspired by the wing motion of birds and insects during flight [34,35], making it well-suited for harvesting the hydrokinetic energy [36]. At present, the most of flapping wing generators employ linkage mechanisms, hydraulic transmissions, and pulley mechanisms to coordinate the flapping and pitching motion for stable operation [37–39]. The coordination generates the kinematic coupling between the flapping and pitching of the flapping wing. However, the existing flapping wing generator still has been limited on harvesting low-velocity water flow energy due to the kinematic coupling between the pitching and flapping motions. Furthermore, the savonius airfoil has excellent automatic pitching characteristics, namely easy rotation under fluid driving [40], which makes it possible to decouple the flapping and pitching of the flapping wing. Therefore, the integration of savonius airfoil and flapping wing can increase the energy harvesting capacity in low-velocity water flow. Compared to the electrical output characteristics of high current and low voltage in electromagnetic generators (EMGs) [41], TENGs have the electrical output characteristics of high voltage and low current [42]. Therefore, the combination of the TENG and the EMG contributes to the diversification of electrical output characteristics.

In this study, for harvesting hydrokinetic energy of unidirectional low-velocity current, a novel savonius flapping wing triboelectric-electromagnetic hybrid generator (SFW-TEHG) is designed specifically by combining the savonius airfoil with the flapping wing for the first time. The SFW-TEHG consists of a savonius flapping wing, a pitching mechanism, a transmission mechanism, and an energy conversion part that includes a TENG and an electromagnetic generator (EMG). The SFW-TEHG achieves a novel operation pattern. In the operation pattern, the savonius flapping wing moves back and forth by the pitching mechanism automatically adjusting its attack angle and enabling it to generate alternating lift in the water flow. Moreover, the transmission mechanism efficiently converts the low-frequency flapping of the SFW into high-frequency unidirectional rotating of the energy conversion part. Under the water velocity of 0.21 m/s, the TENG attains the open-circuit voltage peak of 1.57 kV and the short-circuit current peak of 30.94 μA, the EMG attains the open-circuit voltage peak of 6.24 V and the short-circuit current peak of 3.76 mA. Considering that many monitoring devices are widely used in agricultural production, a power supply system based on the SFW-TEHG is built, which can power successfully a wireless temperature sensor and a wireless light sensor by harvesting hydrokinetic energy in a water channel simulator, respectively. These sensors can transmit temperature and luminous flux information to different receivers. These provide a novel method for solving the power supply difficulty of distributed microsensors in the agriculture field.

2. Results and discussion

2.1. Structural design and operation principle of SFW-TENG

The application background of the SFW-TEHG, harvesting the hydrokinetic energy of water flow in a water channel of the farmland for powering sensors that monitor the environment, is shown in Fig. 1(a). The SFW-TEHG is constituted by a savonius flapping wing (SFW), a pitching mechanism, a transmission mechanism, an energy conversion part, a pair of brakes, and a frame, as shown in Fig. 1(b). Furthermore, the photograph of the SFW-TEHG and its components are exhibited in Fig. S1. The detail of SFW is depicted in Fig. S2(a). The pitching mechanism consists of three racks, two gears, a stopper, and six magnets. It can control the SFW pitching angle which is the included angle between the chord line of the SFW and the water flow direction shown in Fig. S2(a)(ii). The transmission mechanism is composed of a shaft, two homologous one-way clutches, two racks in opposite arrangements, and a set of sliding rails and sliders. The structural characteristics of the shaft and the two one-way clutches are illustrated in Fig. S2(b). The structure parameters of the primary parts in the transmission mechanism are illustrated in Table S1. Furthermore, the function of the transmission mechanism is the converting the flapping of the SFW into the unidirectional rotation of the shaft. The energy conversion part includes a rotor, a TENG, and an EMG. The rotor is fixed in the shaft, loading the FEP films in the TENG and the magnets in the EMG. Thus, the function of the energy conversion part is to transform the rotational kinetic energy of the shaft into electricity.

Fig. 1(c) illustrates the motion states of the SFW-TEHG in a cycle. In the original form, the SFW is locked at a set pitching angle through the pitching mechanism and moves left through the driving force of the water flow, as depicted in Fig. 1(c)(i). Meanwhile, the rack 1 and one-way clutch 1 transform the flapping of the SFW into the clockwise rotation of the shaft. When the SFW moves to the left limit position, the rack 5 is pushed by the left brake, and then drives the rack 3 to move up and rack 4 to move down. With the rack 3 moving up, the SFW is unlocked and rotates clockwise by the driving force of the water flow until the SFW rotates to another set pitching angle and is locked again by the rack 4, as shown in Fig. 1(c)(ii). During the SFW rotation, its lift changes gradually. When the lift direction of the SFW is towards the right, the SFW moves towards the right. The rack 2 and one-way clutch 2 transform the flapping of the SFW into the clockwise rotation of the shaft at the same time, as shown in Fig. 1(c)(iii). When the SFW moves to the right limit position, the rack 5 is pushed by the right brake, and drives the rack 4 to move up and rack 3 to move down. With the rack 4 moving up, the SFW is unlocked and rotates clockwise by the driving force of the water flow until it rotates again to the original pitching angle and is locked again by the rack 3, as exhibited in Fig. 1(c)(iv). Likewise, the SFW moves towards the left when the lift direction of the SFW is towards the left. So far, the SFW has completed one cycle motion. The more detailed operation states and force analysis of the SFW-TEHG are shown in Fig. S3. Furthermore, during the operation of the SFW, the shaft drives

the TENG and EMG, and transforms the rotational kinetic energy of the shaft into electrical power. Fig. S4 illustrates the relative operation principles and the simulations of the TENG and the EMG.

To explore the motion performances of the SFW, a series of numerical simulations is conducted, Fluent is employed to simulate the SFW motion in water, as shown in Fig. 2. The base line length H and the pitching angle θ are selected to study their influence on the motion performance of the SFW. The details of the two parameters are exhibited in Fig. 2(a). The preprocessing of the numerical simulation is depicted in Fig. S5. Fig. 2(b) illustrates that the flapping frequency and mean flapping velocity of the SFW increase initially and decrease then with the increases of the base line length H. At the base line length H of 60 mm, these two parameters reach their peak values. Subsequently, it is indicated in the research of the pitching angle θ at the base line length H of 60 mm that the two performance parameters also increase initially and decrease then with the pitching angle θ increasing. At the pitching angle θ of 70°, the two performance parameters attain their peak values. Fig. 2(c) depicts the pressure fields around these SFWs, which are taken respectively in a stable motion cycle from their corresponding numerical simulations.

In Fig. 2(c)(i), it is found that at the base line length H of 60 mm, a larger high-pressure area exists on the lower surface of the SFW leading edge at $t = 0.3$ s, which promotes the SFW to move and thus enhances the flapping velocity of the SFW. Its faster flapping velocity also is demonstrated by its longer movement distance than these other SFWs at the same time of $t = 1.9$ s, which enables the SFW to convert more hydrokinetic energy into its mechanical energy. Fig. 2(c)(ii) depicts the pressure around the SFWs at different pitching angles and the fixed base line length H of 60 mm. The SFW at the pitching angle θ of 70° and $t = 0.3$ s has a larger high-pressure area on its lower surface of the leading edge than these SFWs with other pitching angles. This promotes the SFW to rapidly move. Additionally, the vorticity fields of these SFWs are shown in Fig. S6. The more clear and detailed real-time flow fields can be watched in Video S2 and Video S3. By integrating the simulating results, the SFW at the base line length H of 60 mm and the pitching angle θ of 70° can transform more hydrokinetic energy into its mechanical energy in the numerical simulations.

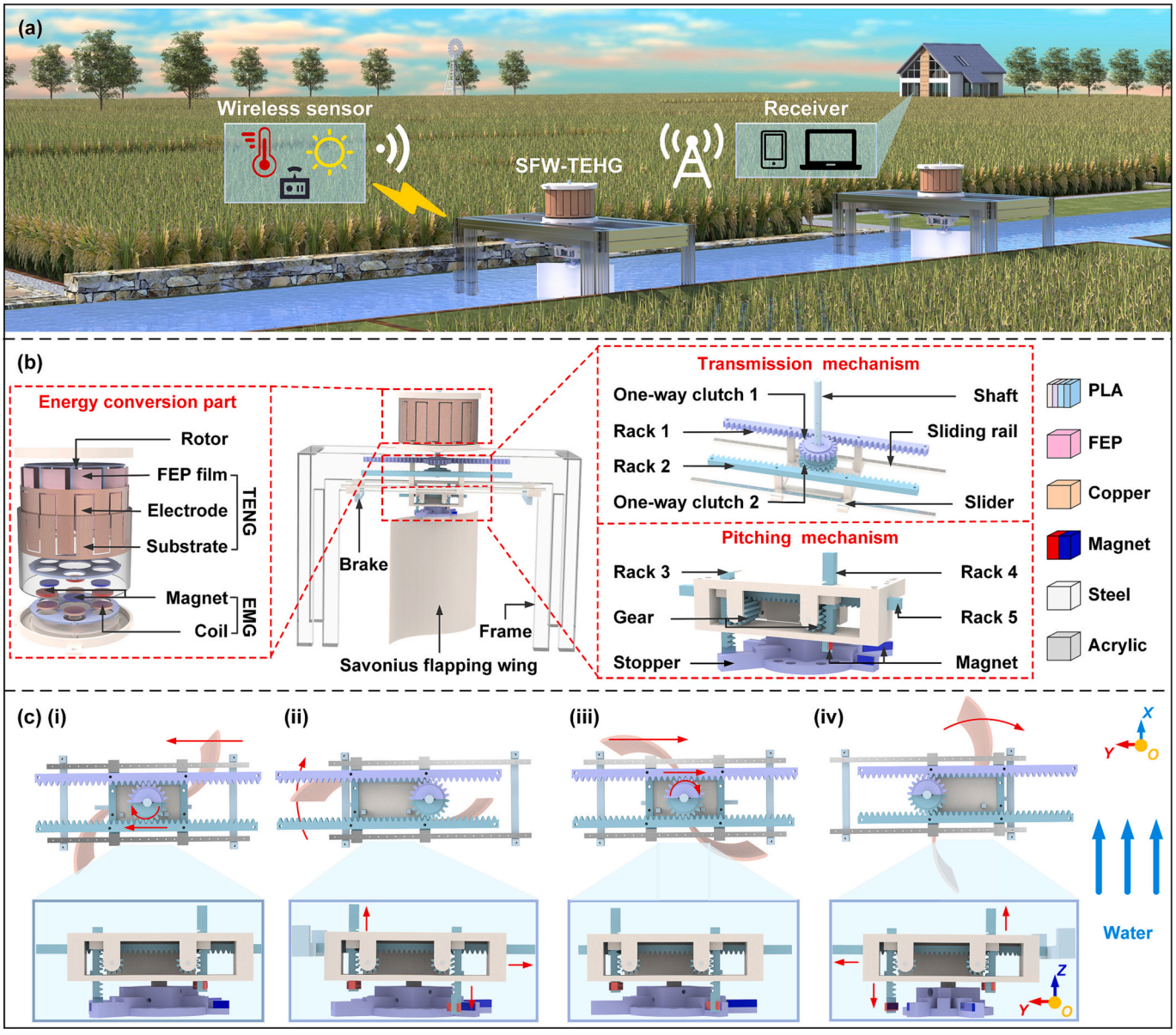

Fig. 1. Structure and operating states of the SFW-TEHG. (a) Channel application prospect of the SFW-TEHG, (b) structure and component of the SFW-TEHG, (c) operating states of the SFW-TEHG.

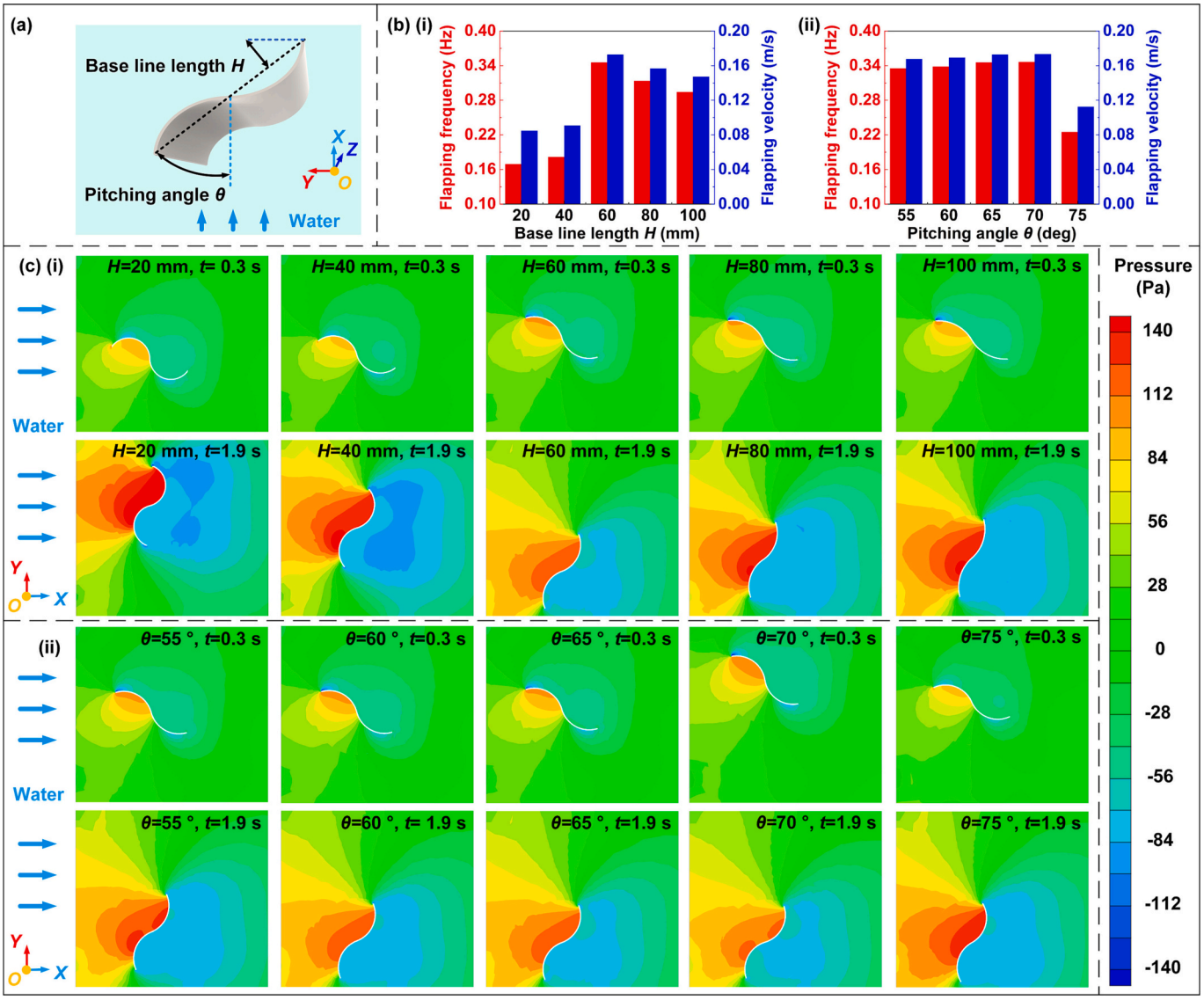

Fig. 2. Numerical simulations of the SFW. (a) Schematic diagram of the base line length H and pitching angles θ, (b) energy harvesting performances of SFW with different base line lengths and different pitching angles, (c) pressure field around the flapping wing.

2.2. Output performance of SFW-TEHG

The energy conversion part influences strongly the electrical output performance of the SFW-TEHG. Herein, an experiment platform in which a linear motor is employed for simulating the SFW flapping is constructed and shown in Fig. 3(a)(i). The research on the internal structures of the TENG is conducted first. To make the research of the TENG more universal, the two internal parameters, rotor diameter Φ_1 and FEP film length L_1, are processed to be dimensionless. The rotor diameter Φ_1 is defined by the acrylic substrate diameter Φ_2 and the diameter relation coefficient K_1. The FEP film length L_1 is defined by the copper electrode grid length L_2 and the length relation coefficient K_2. The relevant details of these definitions are depicted in Fig. 3(a)(ii). The two coefficients, K_1 and K_2, are used to study their influence on the electrical output performances of the TENG, as exhibited in Fig. 3 (b) and Fig. S7. It can be found that the open-circuit voltage V_{OC}, the short-circuit current I_{SC}, and the transferred charge Q_{SC} of the TENG exhibit the same trend with the changes of K_1 and K_2. When the diameter relation coefficient K_1 is 0.88, these electrical performance parameters enhance with the increase of the length relation coefficient K_2. When the diameter relation coefficient K_1 is 0.92, these electrical performance parameters increase initially and decrease then with the increase of the length relation coefficient K_2, reaching the optimal value at the length relation coefficient K_2 of 2.4. When the diameter relation coefficient K_1 is 0.96, these electrical performance parameters decrease with the increase of the length relation coefficient K_2. This is because each FEP film contacts integrally a copper electrode at the K_1 of 0.92 and the K_2 of 2.4. On this basis, the increase of the two coefficients will result in the FEP film contacting simultaneously two copper electrodes, while the decrease of the two coefficients will result in their contact area reducing. These two results lead to the performance reduction of the TENG. Therefore, the K_1 of 0.92 and K_2 of 2.4 are applied in the following research. Fig. S8 illustrates the influence of the distance between the magnets and the coils on the electrical performances of the EMG, and Fig. S8(a) depicts the experimental platform. Fig. S8(b) exhibits that the electrical performances of the EMG decrease as the distance increases. Therefore, the appropriate minimum distance of 2 mm is applied. In addition, the reciprocating frequency f_{rec} is a vital factor affecting the electrical performance of TENG and EMG. Therefore, five reciprocating frequencies f_{rec} (0.10 Hz, 0.15 Hz, 0.20 Hz, 0.25 Hz, 0.30 Hz,) are selected to study the reciprocating frequency influence on electrical performance of TENG and EMG. The motion equations and motion

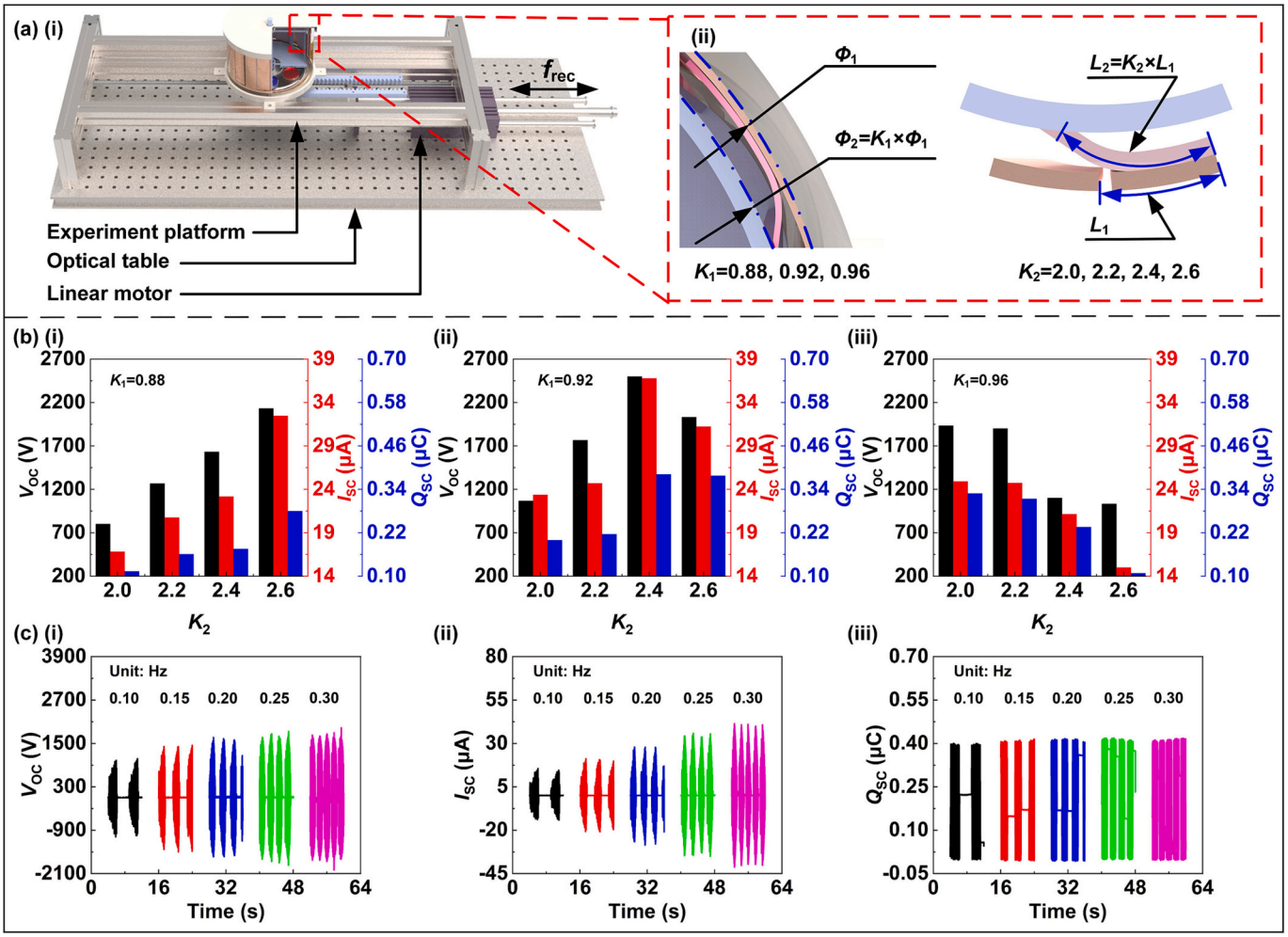

Fig. 3. Electrical performances of the TENG at different internal structures and the different external stimulations. (a) Experimental platform, (b) electrical performances of the TENG at different diameter relation coefficients K_1 and length relation coefficients K_2, (c) electrical performance of the TENG at different external stimulations.

parameters of the linear motor under different reciprocating frequencies f_{rec} are depicted in eqs. (S7) and (S8) and Table S2, respectively. The research results are illustrated in Fig. 3(c) and Fig. S8(c), respectively. The electrical performances of the TENG increase with the f_{rec} increasing. The electrical performances of the EMG appear a similar trend. In addition, Fig. S9 depicts that two durability experiments are conducted at the f_{rec} of 0.6 Hz. The I_{SC} of the TENG drops to 88%, and the I_{SC} of the EMG remains constant almost after they operate for 100,000 cycles.

To more directly research the influence of the SFW on the output performances of the SFW-TEHG, the SFW-TEHG is tested with the different base line lengths and pitching angles in water velocity of 0.45 m/s, and the test results are shown in Fig. 4. The implementation methods and the specific structures of the different base line lengths and pitching angles are depicted in Fig. S10. Figs. 4(a) and (b) show the frequencies (mean value) of the rotor and the SFW. The frequency of the rotor is higher than the frequency of SFW at whole base line lengths and pitching angles. This demonstrates that the transmission mechanism can transform the low-frequency flapping of the SFW into the high-frequency rotating of the rotor. In addition, the flapping frequency of the SFW increases initially and decreases then with the H increasing at a temporary θ of 65°, and reaches a peak at the base line length H of 60 mm. Similarly, the flapping frequency of the SFW increases initially and decreases then with the θ increasing at the fixed H of 60 mm, and reaches a peak of 0.27 at the pitching of 70°. This flapping frequency increases by 22.67% more than that of the relatively common SFW with the H of 20 mm and the θ of 65°. These indicate that the SFW at the H of 60 mm and the θ of 70° can harvest more hydrokinetic energy by its flapping. These trends are almost similar to the above numerical simulations. Later, the electrical output performances of the SFW-TEHG are tested and shown in Figs. 4(b-d), and Fig. S11. The electrical output performances of the SFW-TEHG exhibit the same trends as the flapping frequency of the SFW and the rotation frequency of the rotor. At the base line length H of 60 mm and the pitching angle θ of 70°, the electrical performances of the TENG reach the optimizations, the V_{OC} peak of 1.72 kV, the I_{SC} peak of 34.57 μA, and the Q_{SC} peak of 0.43 μC. At the same configuration, the EMG also achieves optimal electrical performances, the V_{OC} peak of 7.47 V and the I_{SC} peak of 3.33 mA. Therefore, the following experiments employ the fixed parameter combination, the base line length H of 60 mm and the pitching angle θ of 70°.

To explore the electrical output performances of the SFW-TEHG in the low-velocity water flow, the SFW-TEHG is tested under the water velocity range of 0.21–0.64 m/s, as shown in Fig. 5 and Fig. S12. Fig. 5 (a) and Fig.S12(a) illustrate that the V_{OC} peak, the I_{SC} peak, and the Q_{SC} peak of the TENG is 1.56 kV to 2.20 kV, 29.39 μA to 48.70 μA and 0.42 μC to 0.45 μC under the water velocity range of 0.21–0.64 m/s, respectively. In addition, Fig. S12(b)(i) and Fig. 5(a)(iii) respectively depict the current and output power of the TENG under different external resistances, and then the appropriate external resistance is confirmed as 100 MΩ. At the external resistance, the peak power of the

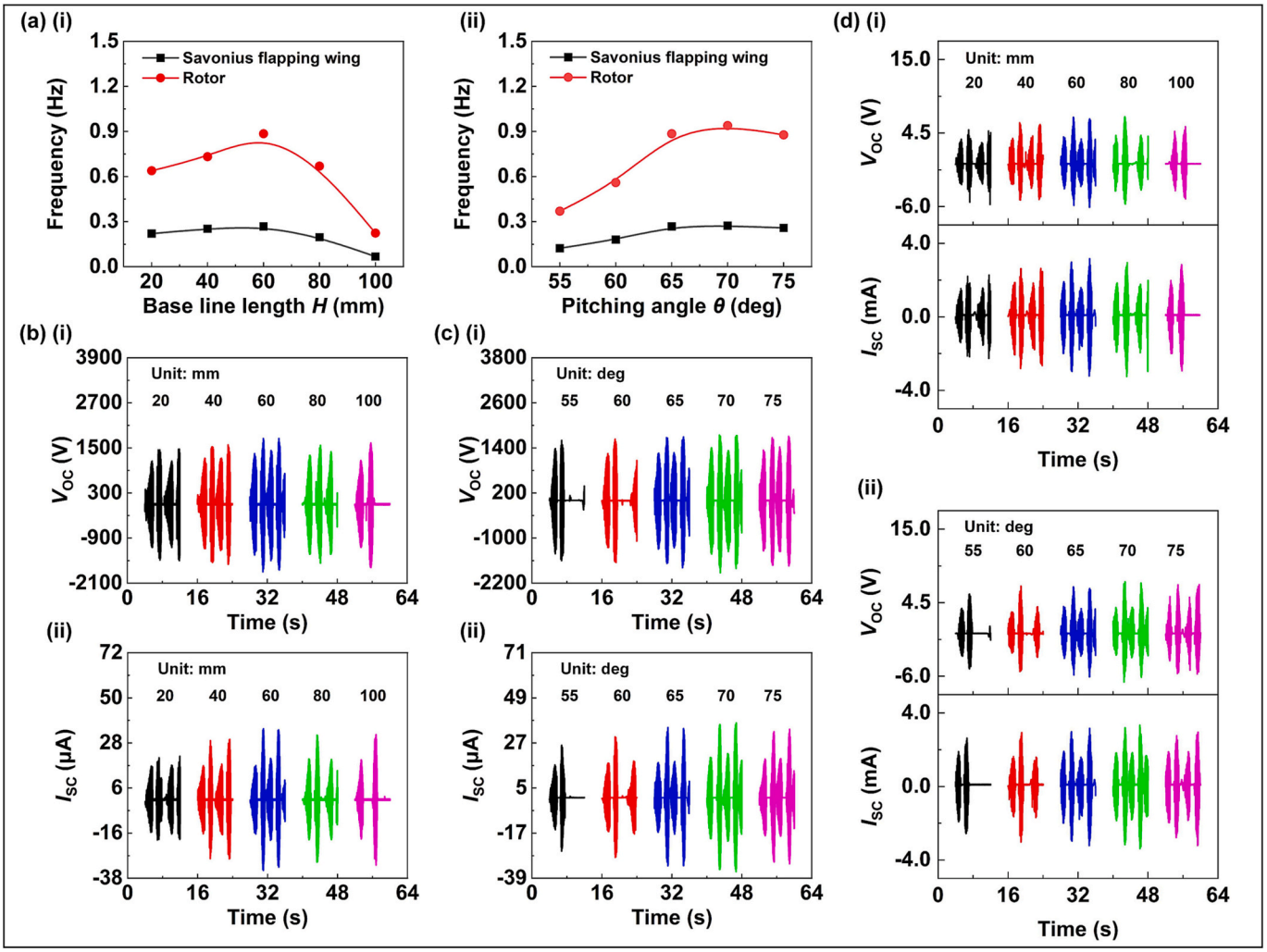

Fig. 4. Electrical output performances of the SFW-TEHG at diverse wing structure parameters. (a) Frequency of flapping wing and rotor with different wing base line lengths and pitching angles, (b) electrical performance of the TENG at the diverse base line lengths and pitching angles, (c) electrical performance of the EMG at the diverse base line lengths and pitching angles.

TENG is 24.44 mW to 37.28 mW under the water velocity range of 0.21–0.64 m/s. Moreover, the V_{OC} peak and I_{SC} peak of the EMG are respectively 6.22 V to 10.68 V and 3.76 mA to 5.43 mA, as shown in Fig. 5(b). Fig. S12(b)(ii) and Fig. 5(b)(iii) respectively depict the current and output power of the EMG under different external resistances. The peak power of the EMG is 4.35 mW to 9.36 mW at its external resistance of 1000 Ω, under the water velocity range of 0.21–0.64 m/s. Subsequently, Fig. 5(c) shows that a series of charging capacitor experiments are conducted under the water velocity of 0.31 m/s. It is found that the TENG charges slowly these capacitors, but the voltage rise speeds of the capacitors are almost constant. The EMG can charge rapidly these capacitors. However, when the capacitor voltage reaches a certain threshold, it will not increase with the increase of time. For example, when the voltage of the 10 μF capacitor reaches 9.64 V, the voltage almost cannot increase with the increase of charging time. Hence, to combine their strengths, the TENG and the EMG are utilized together for charging capacitors. Compared to the adopted TENG alone, it allows for faster charging. Compared to the adopted EMG alone, it can charge the capacitor voltage to a higher level. Therefore, the combining of TENG and the EMG enables the SFW-TEHG to satisfy the requirements of higher voltage and charge speed, which can increase the range of potential applications.

2.3. Application demonstration of SFW-TEHG

In agricultural production, a large number of electronic products is used to provide convenience for farmers, such as lighting device, monitoring device, and more. Specially, adjusting crop cultivation methods according to environmental changes can effectively enhance crop yields, which enable environmental monitoring devices such as temperature sensor and light intensity sensor to be particularly important in agricultural production. Therefore, three application experiments that the SFW-TEHG is utilized to power lighting devices and environmental monitoring devices are conducted in a water channel under the water velocity of 0.31 m/s, as depicted in Fig. 6 and Videos S4-S6. In Fig. 6(a), the SFW-TEHG lightens successfully 666 LEDs. Whereafter, a circuit is designed and employed in the following two experiments to transmit the electricity of the SFW-TEHG into sensors, as shown in Fig. 6(b). From Fig. 6(c), the SFW-TEHG can power a wireless temperature sensor to monitor the environment temperature. When the voltage of the 10 mF capacitor used in the circuit is charged to 3.7 V, the wireless temperature sensor begins to operate and transmits the temperature information to a mobile receiver. The specific process can be watched in Video S5, and the technical parameters of the wireless temperature sensor are illustrated in Table S3. Fig. 6(d) depicts that the SFW-TEHG can drive a wireless light sensor for monitoring the luminous flux. When the voltage of the 4.7 mF capacitor used in the circuit is

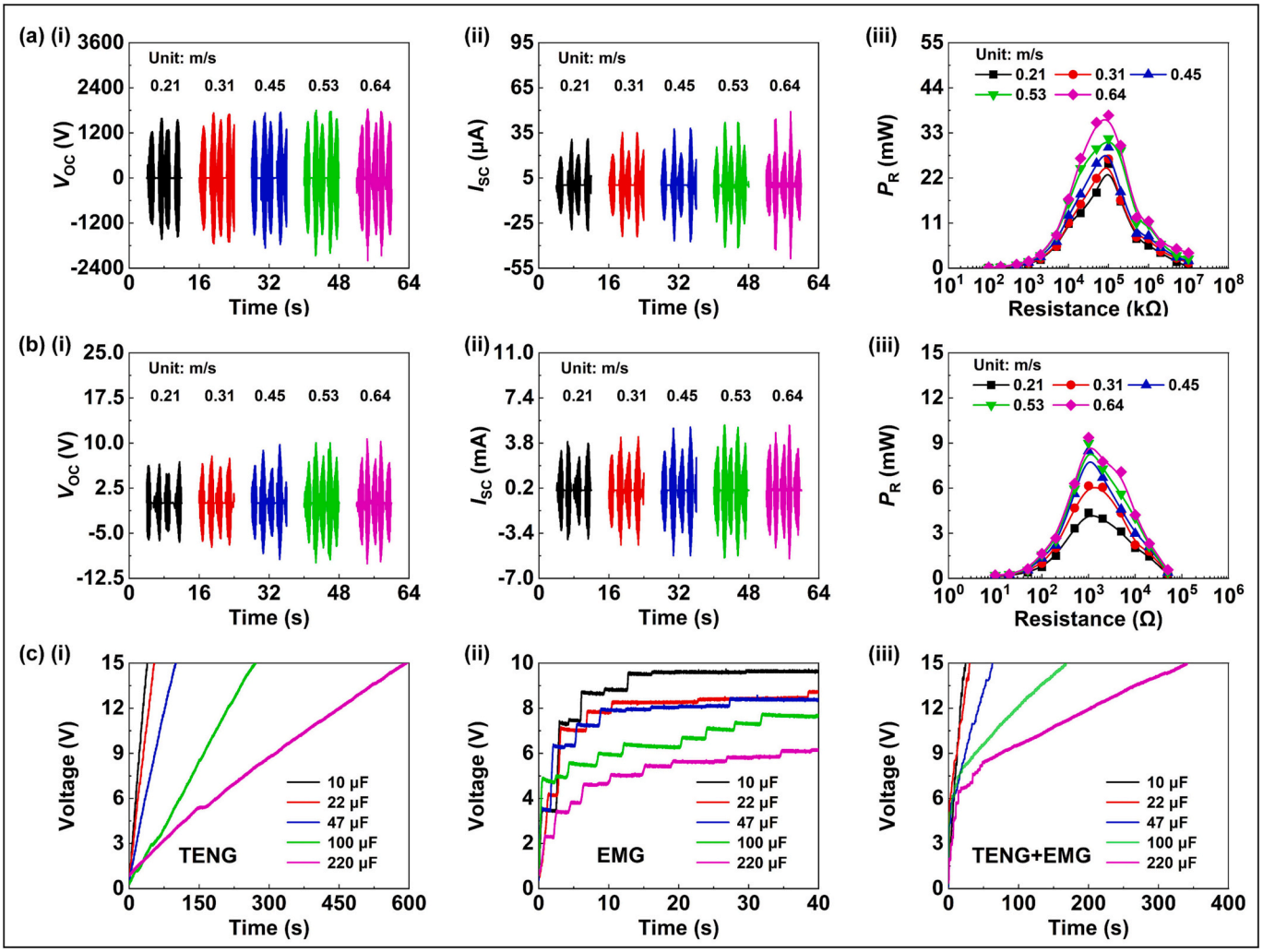

Fig. 5. Electrical output performances of the SFW-TEHG under diverse flow velocities and charging capacities experiment of SFW-TEHG under a fixed water velocity of 0.31 m/s. (a) Electrical performances of TENG under diverse water velocities, (b) electrical performances of EMG under diverse water velocities, (c) charging capacities of SFW-TEHG under a fixed water velocity of 0.31 m/s.

charged to 3.7 V, the wireless light sensor begins to operate and transmit the luminous flux information to a receiver. The specific process can be watched in Video S6, and the technical parameters of the wireless light sensor are illustrated in Table S3.

3. Conclusions

In summary, the SFW-TEHG was proposed to harvest low-velocity water flow energy. The SFW-TEHG implemented a novel movement pattern of the SFW. At the movement pattern, the attack angle of the SFW was changed to generate alternating lift by the pitching mechanism of the SFW-TEHG for realizing its reciprocating flapping in water flow. Whereafter, the transmission mechanism converted the low-frequency flapping of the SFW into the high-frequency unidirectional rotating of the rotor in the energy conversion part, thereby accomplishing the conversion of hydrokinetic energy into electricity. Later, the relative numerical simulations were conducted to explore the motion states of the SFW in the water flow and the fluid state around the SFW. In the parameter experiment, the internal parameters of the TENG and the EMG in the energy conversion part and the structure parameters of the SFW are optimized to enhance the output performances. Under the water velocity of 0.45 m/s, the flapping frequency of the optimized SFW with the chord line length of 60 mm and pitching angle θ of 70° attained 0.27 Hz and increased by 22.67% more than that of the relatively common SFW with the line length of 20 mm and pitching angle θ of 65°. In addition, the rotation frequencies of the TENG and EMG attained 0.92 Hz, which verified the increase of the frequency achieved by the transmission mechanism. Under the water velocity of 0.21 m/s, the TENG achieved the V_{OC} peak of 1.57 kV and the I_{SC} peak of 30.94 μA. The EMG realized the V_{OC} peak of 6.24 V and the I_{SC} peak of 3.76 mA under the same water velocity. In the application exhibition, the SFW-TEHG was employed to lighten LED lights and drive the wireless sensors that monitored the temperature and the luminous flux. The SFW-TEHG offers a novel approach for the harvesting of low-velocity hydrokinetic energy and the power supply of distributed microsensors.

4. Experiment section

Fabrication of the SFW-TEHG: The SFW-TEHG comprises a savonius flapping wing, a pitching mechanism, a transmission mechanism, and an energy conversion part comprising a TENG and an EMG. The savonius flapping wing is manufactured using 3D printing with PLA materials. Its height is 250 mm, and its chord length is 250 mm. The pitching and the transmission mechanism are manufactured by 3D printing and standard components. The energy conversion part (150 × 150 × 110 mm) is manufactured by copper film, FEP film, magnet, copper coil, acrylic bucket, and 3D printing.

Electrical measurement: A linear motor (LinMot-BHM01–48,

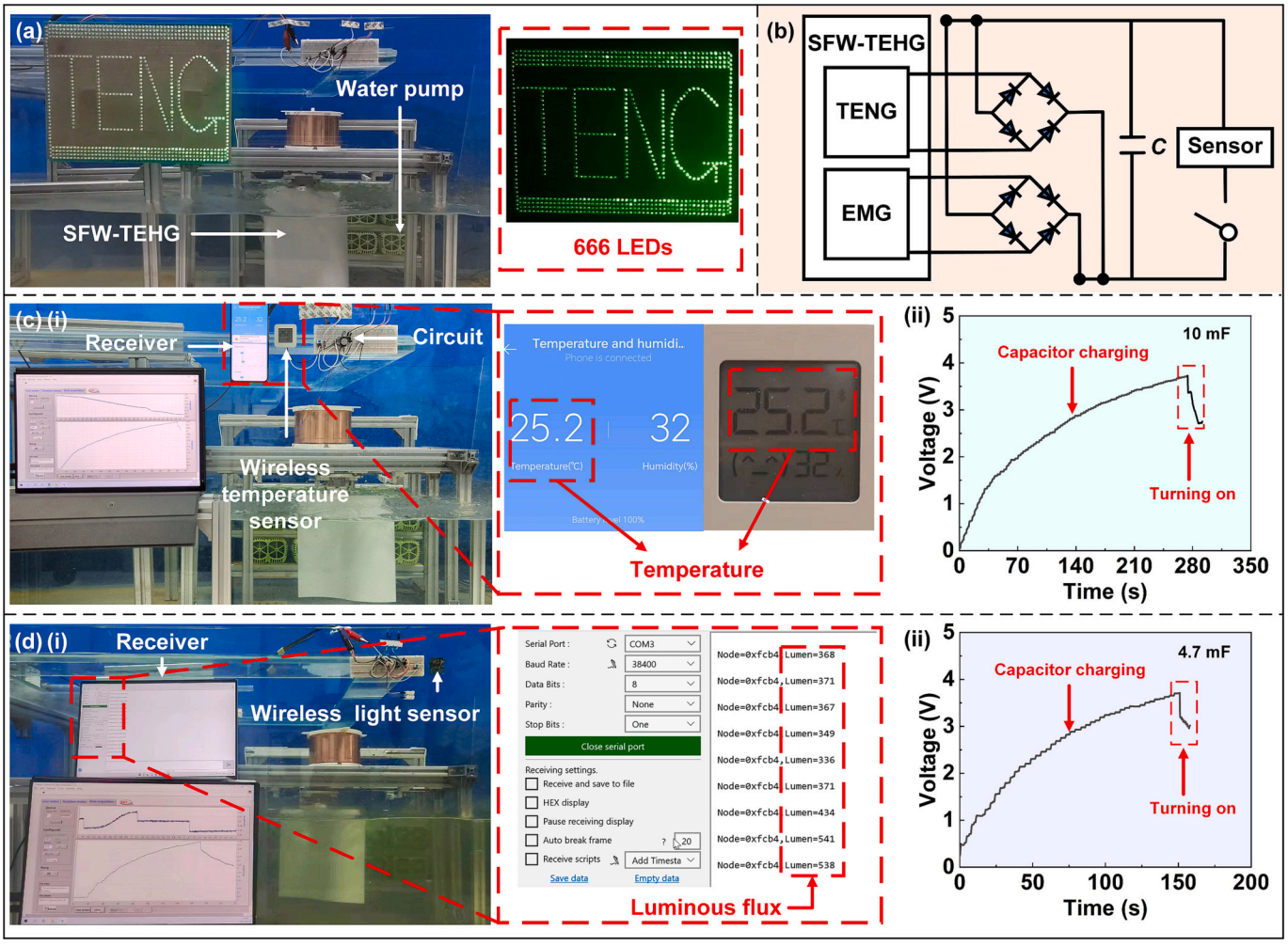

Fig. 6. Application of the SFW-TEHG under the water velocity of 0.31 m/s. (a) 666 LEDs powered by the SFW-TEHG under the water velocity of 0.31 m/s, (b) power supply circuit, (c) wireless temperature sensor powered by the SFW-TEHG under the water velocity of 0.31 m/s, (d) wireless light sensor powered by the SFW-TEHG under the water velocity of 0.31 m/s.

Switzerland) is used to simulate the flapping wing motion. A water flow environment is simulated by 8 water pumps (YQ, 55 W, China). The water velocity is measured using a kinemometer (LS300-A, Zhuoma, China). An electrometer (6514, Keithley, USA) is utilized to measure the I_{SC} and Q_{SC}. An oscillograph (DS2202A, RIGOL, China) is utilized to measure the V_{OC}.

Supplementary data to this article can be found online at https://doi.org/10.1016/j.apenergy.2023.122512.

CRediT authorship contribution statement

Jiacheng Zhang: Writing – original draft, Investigation, Conceptualization. **Yang Yu:** Writing – original draft, Supervision, Investigation. **Hengyu Li:** Validation, Investigation. **Mingkang Zhu:** Validation, Investigation. **Sheng Zhang:** Validation, Investigation. **Chengjie Gu:** Validation. **Lin Jiang:** Investigation. **Zhong Lin Wang:** Writing – review & editing, Resources, Funding acquisition. **Jianyang Zhu:** Writing – review & editing, Resources, Conceptualization. **Tinghai Cheng:** Writing – review & editing, Resources, Conceptualization.

Declaration of Competing Interest

The authors declare that they have no known competing financial interests or personal relationships that could have appeared to influence the work reported in this paper.

Data availability

Data will be made available on request.

Acknowledgments

The authors are grateful for the support from the National Natural Science Foundation of China (project No. 51975429), and the National Key R & D Project from Minister of Science and Technology (Nos. 2021YFA1201601 & 2021YFA1201604).

References

[1] Cao X, Xiong Y, Sun J, Xie X, Sun Q, Wang ZL. Multidiscipline applications of triboelectric nanogenerators for the intelligent era of internet of things. Nano-Micro Lett 2023;15:14. https://doi.org/10.1007/s40820-022-00981-8.
[2] Chang A, Uy C, Xiao X, Xiao X, Chen J. Self-powered environmental monitoring via a triboelectric nanogenerator. Nano Energy 2022;98:107282. https://doi.org/10.1016/j.nanoen.2022.107282.
[3] Wang ZL. Entropy theory of distributed energy for internet of things. Nano Energy 2019;58:669–72. https://doi.org/10.1016/j.nanoen.2019.02.012.
[4] Mrozik W, Rajaeifar MA, Heidrich O, Christensen P. Environmental impacts, pollution sources and pathways of spent lithium-ion batteries. Energy Environ. Sci. 2021;14:6099–121. https://doi.org/10.1039/D1EE00691F.
[5] Fouz DM, Carballo R, López I, Iglesias G. A holistic methodology for hydrokinetic energy site selection. Appl. Energy 2022;317:119155. https://doi.org/10.1016/j.apenergy.2022.119155.
[6] Li W, Chen X. Powering body area sensor networks matter 2020;2:1085–6. https://doi.org/10.1016/j.matt.2020.04.006.

[7] Ahmed A, Saadatnia Z, Hassan I, Zi Y, Xi Y, He X, et al. Self-powered wireless sensor node enabled by a duck-shaped triboelectric Nanogenerator for harvesting water wave energy. Adv. Energy Mater. 2017;7:1601705. https://doi.org/10.1002/aenm.201601705.

[8] Zhang S, Jing Z, Wang X, Zhu M, Yu X, Zhu J, et al. Soft-bionic-fishtail structured triboelectric nanogenerator driven by flow-induced vibration for low-velocity water flow energy harvesting. Nano Res. 2023;16:466–72. https://doi.org/10.1007/s12274-022-4715-6.

[9] Escuder-Bueno I, Castillo-Rodríguez JT, Zechner S, Jöbstl C, Perales-Momparler S, Petaccia G. A quantitative flood risk analysis methodology for urban areas with integration of social research data. Nat. Hazards Earth Syst. Sci. 2012;12:2843–63. https://doi.org/10.5194/nhess-12-2843-2012.

[10] Lin L, Xie Y, Niu S, Wang S, Yang P-K, Wang ZL. Robust triboelectric Nanogenerator based on rolling electrification and electrostatic induction at an instantaneous energy conversion efficiency of ~55%. ACS Nano 2015;9:922–30. https://doi.org/10.1021/nn506673x.

[11] Fan F-R, Tian Z-Q, Lin Wang Z. Flexible triboelectric generator. Nano Energy 2012;1:328–34. https://doi.org/10.1016/j.nanoen.2012.01.004.

[12] Wang ZL. On Maxwell's displacement current for energy and sensors: the origin of nanogenerators. Mater. Today 2017;20:74–82. https://doi.org/10.1016/j.mattod.2016.12.001.

[13] Wang ZL. On the first principle theory of nanogenerators from Maxwell's equations. Nano Energy 2020;68:104272. https://doi.org/10.1016/j.nanoen.2019.104272.

[14] Wang ZL, Wang AC. On the origin of contact-electrification. Mater. Today 2019;30:34–51. https://doi.org/10.1016/j.mattod.2019.05.016.

[15] Wang ZL, Jiang T, Xu L. Toward the blue energy dream by triboelectric nanogenerator networks. Nano Energy 2017;39:9–23. https://doi.org/10.1016/j.nanoen.2017.06.035.

[16] Chung S-H, Son J, Cha K, Choi M, Jung H, Kim M-K, et al. Boosting power output of fluttering triboelectric nanogenerator based on charge excitation through multi-utilization of wind. Nano Energy 2023;111:108389. https://doi.org/10.1016/j.nanoen.2023.108389.

[17] Tang S, Chang W, Li G, Sun J, Du Y, Hui X, et al. High performance wide frequency band triboelectric nanogenerator based on multilayer wave superstructure for harvesting vibration energy. Nano Res. 2023;16:6933–9. https://doi.org/10.1007/s12274-023-5476-6.

[18] Liu Y, Chen B, Li W, Zu L, Tang W, Wang ZL. Bioinspired triboelectric soft robot driven by mechanical energy. Adv. Funct. Mater. 2021;31:2104770. https://doi.org/10.1002/adfm.202104770.

[19] Zhao D, Zhuo J, Chen Z, Wu J, Ma R, Zhang X, et al. Eco-friendly in-situ gap generation of no-spacer triboelectric nanogenerator for monitoring cardiovascular activities. Nano Energy 2021;90:106580. https://doi.org/10.1016/j.nanoen.2021.106580.

[20] Li Y, Guo Z, Zhao Z, Gao Y, Yang P, Qiao W, et al. Multi-layered triboelectric nanogenerator incorporated with self-charge excitation for efficient water wave energy harvesting. Appl. Energy 2023;336:120792. https://doi.org/10.1016/j.apenergy.2023.120792.

[21] Yu Y, Li H, Zhao D, Gao Q, Li X, Wang J, et al. Material's selection rules for high performance triboelectric nanogenerators. Mater. Today 2023;64:61–71. https://doi.org/10.1016/j.mattod.2023.03.008.

[22] Chen A, Zhang C, Zhu G, Wang ZL. Polymer materials for high-performance triboelectric Nanogenerators. Adv Sci 2020;7:2000186. https://doi.org/10.1002/advs.202000186.

[23] Han J, Feng Y, Chen P, Liang X, Pang H, Jiang T, et al. Wind-driven soft-contact rotary triboelectric nanogenerator based on rabbit fur with high performance and durability for smart farming. Adv. Funct. Mater. 2022;32:2108580. https://doi.org/10.1002/adfm.202108580.

[24] Zhao Z, Zhou L, Li S, Liu D, Li Y, Gao Y, et al. Selection rules of triboelectric materials for direct-current triboelectric nanogenerator. Nat. Commun. 2021;12:4686. https://doi.org/10.1038/s41467-021-25046-z.

[25] Qi Y, Kuang Y, Liu Y, Liu G, Zeng J, Zhao J, et al. Kirigami-inspired triboelectric nanogenerator as ultra-wide-band vibrational energy harvester and self-powered acceleration sensor. Appl. Energy 2022;327:120092. https://doi.org/10.1016/j.apenergy.2022.120092.

[26] Ankanahalli Shankaregowda S, Sagade Muktar Ahmed RF, Nanjegowda CB, Wang J, Guan S, Puttaswamy M, et al. Single-electrode triboelectric nanogenerator based on economical graphite coated paper for harvesting waste environmental energy. Nano Energy 2019;66:104141. https://doi.org/10.1016/j.nanoen.2019.104141.

[27] Luo H, Liu J, Yang T, Zhang Y, Cao Q. Dipteran flight-inspired bistable triboelectric nanogenerator for harvesting low frequency vibration. Nano Energy 2022;103:107755. https://doi.org/10.1016/j.nanoen.2022.107755.

[28] Zhu M, Zhang J, Wang Z, Yu X, Zhang Y, Zhu J, et al. Double-blade structured triboelectric–electromagnetic hybrid generator with aerodynamic enhancement for breeze energy harvesting. Appl. Energy 2022;326:119970. https://doi.org/10.1016/j.apenergy.2022.119970.

[29] Zhang S, Jing Z, Wang X, Fan K, Zhao H, Wang ZL, et al. Enhancing low-velocity water flow energy harvesting of triboelectric–electromagnetic generator via biomimetic-fin strategy and swing-rotation mechanism. ACS Energy Lett 2022;7:4282–9. https://doi.org/10.1021/acsenergylett.2c01908.

[30] Zhang Q, Li L, Wang T, Jiang Y, Tian Y, Jin T, et al. Self-sustainable flow-velocity detection via electromagnetic/triboelectric hybrid generator aiming at IoT-based environment monitoring. Nano Energy 2021;90:106501. https://doi.org/10.1016/j.nanoen.2021.106501.

[31] Xia R, Zhang R, Jie Y, Zhao W, Cao X, Wang Z. Natural cotton-based triboelectric nanogenerator as a self-powered system for efficient use of water and wind energy. Nano Energy 2022;92:106685. https://doi.org/10.1016/j.nanoen.2021.106685.

[32] Zhou Z, Li X, Wu Y, Zhang H, Lin Z, Meng K, et al. Wireless self-powered sensor networks driven by triboelectric nanogenerator for in-situ real time survey of environmental monitoring. Nano Energy 2018;53:501–7. https://doi.org/10.1016/j.nanoen.2018.08.055.

[33] Deng Z, Xu L, Qin H, Li X, Duan J, Hou B, et al. Rationally structured triboelectric nanogenerator arrays for harvesting water-current energy and self-powered sensing. Adv. Mater. 2022;34:2205064. https://doi.org/10.1002/adma.202205064.

[34] Wissa A. Birds trade flight stability for manoeuvrability. Nature 2022;603:579–80. https://doi.org/10.1038/d41586-022-00638-x.

[35] McKinney W, DeLaurier J. Wingmill: an oscillating-wing windmill. J Energy 1981;5:109–15. https://doi.org/10.2514/3.62510.

[36] Teng L, Deng J, Pan D, Shao X. Effects of non-sinusoidal pitching motion on energy extraction performance of a semi-active flapping foil. Renew. Energy 2016;85:810–8. https://doi.org/10.1016/j.renene.2015.07.037.

[37] Kinsey T, Dumas G, Lalande G, Ruel J, Méhut A, Viarouge P, et al. Prototype testing of a hydrokinetic turbine based on oscillating hydrofoils. Renew. Energy 2011;36:1710–8. https://doi.org/10.1016/j.renene.2010.11.037.

[38] Ma P, Wang Y, Xie Y, Han J, Sun G, Zhang J. Effect of wake interaction on the response of two tandem oscillating hydrofoils. Energy Sci Eng 2019;7:431–42. https://doi.org/10.1002/ese3.286.

[39] Kim J, Quang Le T, Hwan Ko J, Ebenezer Sitorus P, Hartarto Tambunan I, Kang T. Experimental and numerical study of a dual configuration for a flapping tidal current generator. Bioinspir Biomim 2015;10:046015. https://doi.org/10.1088/1748-3190/10/4/046015.

[40] Grönman A, Tiainen J, Jaatinen-Värri A. Experimental and analytical analysis of vaned savonius turbine performance under different operating conditions. Appl. Energy 2019;250:864–72. https://doi.org/10.1016/j.apenergy.2019.05.105.

[41] Hong H, Yang X, Cui H, Zheng D, Wen H, Huang R, et al. Self-powered seesaw structured spherical buoys based on a hybrid triboelectric–electromagnetic nanogenerator for sea surface wireless positioning. Energy Environ. Sci. 2022;15:621–32. https://doi.org/10.1039/D1EE02549J.

[42] Yang W, Zhao T, Li Z, Liu B, Tang C, Tian G, et al. Study on the performance of spherical collision triboelectric nanogenerator. Appl. Energy 2023;351:121824. https://doi.org/10.1016/j.apenergy.2023.121824.